

# Characterization of near-field optical microscope probes

Petr Klapetek,<sup>a\*</sup> Miroslav Valtr,<sup>a</sup> Petr Klenovský<sup>a,b</sup> and Jiří Buršík<sup>c</sup>

In this article the far-field radiation analysis of near-field optical probes is presented. It is shown that the quality of probes used for near-field scanning microscopy imaging can be estimated using directional measurements of the far-field radiation patterns. Experimental results are compared with numerical modeling of far-field radiation performed using finite difference in time-domain method (FDTD) and with SEM characterization of real probe geometry. The effects of probe geometry on real measurement on different samples are studied as well. Copyright © 2008 John Wiley & Sons, Ltd.

**Keywords:** near-field scanning optical microscopy; image artefacts; optical analysis

## Introduction

Near-field scanning optical microscopy is a promising and still developing experimental technique that combines scanning-probe methods resolution with imaging and analysis possibilities of optical microscopes.<sup>[1]</sup> Within near-field scanning optical microscopy (NSOM) measurements, the microscope probe is formed by a nanometer-scale light source (or light detector or scatterer) that is scanning over the surface, usually in the constant-gap mode.<sup>[1]</sup>

In most cases, a quantitative optical analysis, i.e. the determination of local optical properties, can be hardly performed using the NSOM instrument as there are too many issues unclear from the experimental point of view. First of all, the exact shape of the NSOM probe is not known and cannot be easily determined during the measurement. Moreover, the electromagnetic field distribution within the probe and in the near-field region as well as the probe's inner geometry is also unknown. As all the information obtained using a NSOM instrument is given by interaction of the electromagnetic field coming from the taper region and the tip-sample interaction volume; topography artifacts that arise from varying near-field electromagnetic distributions over rapidly changing sample topography are very often observed.<sup>[2–7]</sup> Also, this effect cannot be interpreted easily without the knowledge of the exact tip-sample geometry. Finally, topography artifacts can modify or even completely obscure the optical information contained in the data, because of the fact that variations of the sample refractive index and topographic variations can lead to the same effects on the NSOM data.<sup>[8]</sup>

In this article, the NSOM probes are characterized using SEM and far-field radiation measurements. Both methods are compared using numerical modeling of the electromagnetic field radiation using finite difference in time-domain method (FDTD). Finally, theoretical and experimental results obtained measuring simple geometrical structures using NSOM instrument are presented.

## Preparation of Samples and Experimental Arrangements

For NSOM measurements, Aurora 2 NSOM instrument (thermomi-croscopes) was used. Standard metal-shielded fiber tips (Veeco)

with nominal aperture between 80 and 100 nm were used for measurements. All the images were acquired in reflection mode, i.e. the probe was used for local sample illumination and light was collected in the far field by conventional optics. Both shear force topography and optical data were acquired for each scan. As a sample, we used calibration grating (SiO<sub>2</sub> film on silicon substrate having pitch of 8 μm, and height of 180 nm) as a simple example of an object forming topographical artifacts. The sample has a higher slope than the probe slope, the observed slopes therefore correspond to probe slope after a tip-sample convolution. The geometry of the used NSOM probes was measured using an SEM Jeol JSM-6460.

The experimental device used for probe far-field radiation distribution diagram measurements consists of two goniometers driven by stepper motors and a photon counting device (PCD) from SensL company. It is able to measure the far-field radiation diagrams within a hemisphere centered at the NSOM probe aperture. The distance between aperture and detector is 50 mm. The resolution of the acquired radiation diagrams is limited by the very low light intensity out-coming from the probe and consequently by the long acquisition time for a single-point measurement.

## Data Modeling

In order to determine the NSOM probe geometry, we have first used SEM. Using this method, we can analyze the outer probe geometry. However, we still do not have information about the inner geometry, i.e. about the material distribution within the probe. As the probe consists of at least three different materials – transparent core, transparent cladding and aluminium

\* Correspondence to: Petr Klapetek, Czech Metrology Institute, Okružní 31, 638 00 Brno, Czech Republic. E-mail: klapetek@physics.muni.cz

a Czech Metrology Institute, Okružní 31, 638 00 Brno, Czech Republic

b Faculty of Science, Masaryk University, Kotlářská 2, 611 37, Brno, Czech Republic

c Institute of Physics of Materials, CAS, Žitkova 22, 616 62, Brno, Czech Republic

shielding—it can be assumed that the effect of distribution of these materials within the probe affects the NSOM images highly. Note that the effect of aluminium shielding roughness, as observed using SEM as well as the effect of the irregularity of the ideal probe, was negligible compared to the differences between ideal and nonideal probes.

For a simple analysis of these effects, we have developed a simple method based on measurements of far-field probe radiation diagrams. Different directional radiations of broken or modified probes are often observed in real NSOM measurements (e.g. using a video microscope for tip approach). Various defects appearing on the probe apex that are responsible for the electromagnetic field scattering in the near-field region lead to changes in probe radiation in the far field region as well. Therefore, we can expect that the far-field-data analysis significantly helps to reconstruct

the information about both the inner and outer probe geometry that is present completely only in the near-field region.

For the probe radiation modeling, we have used the FDTD.<sup>[9,10]</sup> This method is based on an iterative numerical solution of Maxwell equations which simulate the propagation of a wave in a sequence of very short time steps. For a FDTD computation of radiation diagrams and simulated NSOM reflection images, we have used the following three steps (Fig. 1):

1. optical-fiber probe analysis based on the geometry obtained using SEM and data-sheet-material properties of fiber; computed in a space of  $20 \times 3 \times 3$  wavelengths ( $\lambda = 488$  nm), space discretization of  $\lambda/20$ , using stepping in one-dimension and conformal modeling. This step was performed to validate the electromagnetic field propagation within the modeled

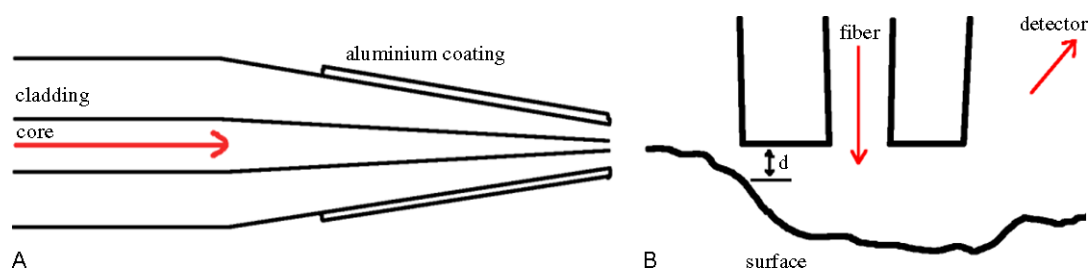


**Figure 1.** (A) Geometry of the modeling of probe radiation. The taper region length is usually up to 1 mm as observed using SEM. The core diameter of  $3.5 \mu\text{m}$ , used in the simulations, corresponds to the single-mode fiber for wavelength of 488 nm used in our experiments. Cladding and metal-film shielding thickness in the taper region (depending on the probe preparation process) were suggested as being  $5\text{--}50 \mu\text{m}$  (cladding) and  $1 \mu\text{m}$  (shielding). (B) Geometry of NSOM image simulation. Locations of the far-field detector used for reflection measurements are in the direction of  $45^\circ$  to the surface normal oriented to the left, right, front and back with respect to the drawing orientation. This figure is available in colour online at [www.interscience.wiley.com/journal/sia](http://www.interscience.wiley.com/journal/sia).

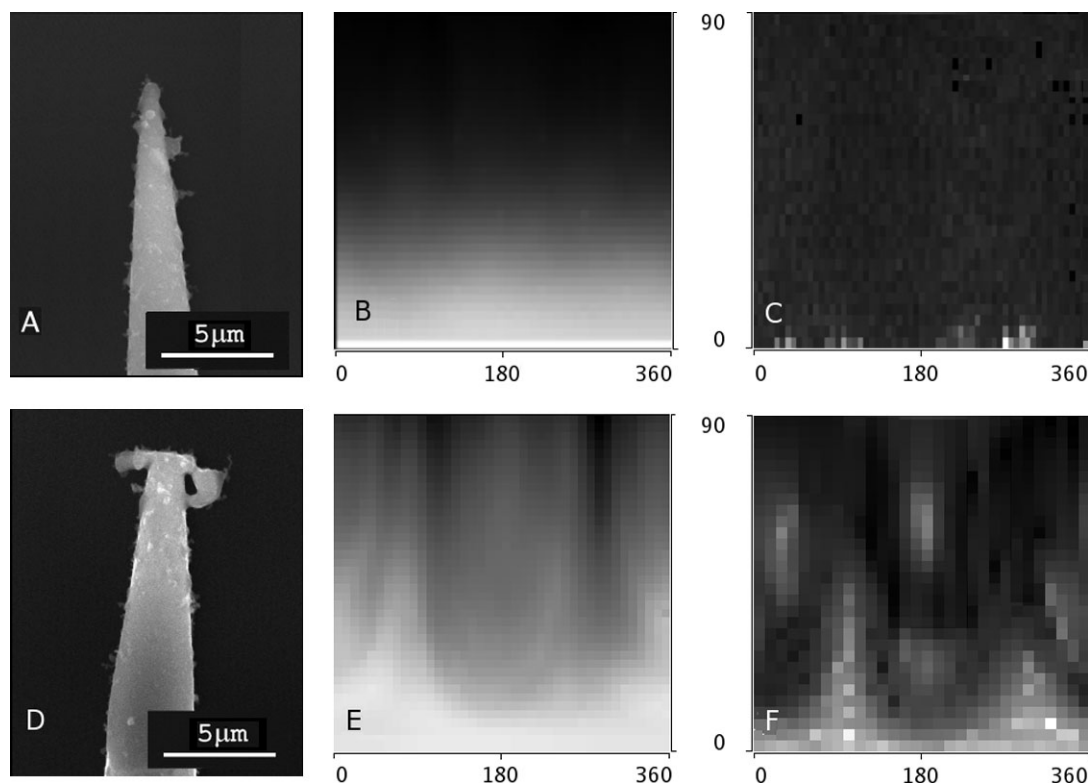


**Figure 2.** (A) New (ideal) probe geometry, (B) simulated and (C) measured far-field radiation diagram, (D) broken-probe geometry, (E) simulated and (F) measured far-field radiation diagram. Far-field radiation diagrams are measured in the range of  $0\text{--}360^\circ$  ( $x$  direction on the image) and  $0\text{--}90^\circ$  ( $y$  direction on the image) covering all the hemisphere.

fiber and to serve as a source for the second step. Note that the discretization value of  $\lambda/20$  is a compromise between computer memory usage and sufficient computation resolution and was determined experimentally.

- probe apex geometry analysis within  $4 \times 4 \times 4 \lambda$ , space discretization  $\lambda/40$ , using near-field to far-field (NFFF)<sup>[11]</sup> computation of the far field limit. The probe outer material geometry was taken from the SEM measurements, the inner geometry was varied to show the dependence of far-field radiation patterns on this parameter. Far-field computation points were located on the hemisphere oriented in the same way as for the experimental measurements of far-field radiation.
- probe-sample interaction analysis within  $4 \times 4 \times 4 \lambda$ , space discretization  $\lambda/20$ , using a NFFF computation of the far field intensity at the location of the NSOM photodetector.

As a result, we have obtained a far-field radiation distribution that is directly comparable with the experimental data measured by the method described in the previous section. We have also obtained modeled NSOM reflection images (after applying the third step for each pixel of the final image) that can be used to compare the computational approach to real NSOM measurements.

## Results and Discussion

In Fig. 2, the image of both an ideal and a nonideal NSOM probe and the corresponding modeled and measured far-field radiation patterns are presented. It can be seen that for the ideal probe, the results of the far-field radiation measurements correspond to expected behavior, i.e. most of the radiations are coming in the direction of the probe orientation (bottom line in the far-field radiation pattern). Note that owing to the extremely low light power coming from the ideal probe the far-field radiation pattern is influenced by the noise as well. For the nonideal probe, we can see much more complicated radiation pattern, both for simulation and measurement. It must be said that the nonideal probe quality was high enough that it could not be distinguished from good probes within regular NSOM measurements probe inspection based on viewing the probe in NSOM CCD camera and checking its total light output. However, as seen both from SEM and far-field radiation measurements, the probe apex is much larger and much more irregular than for ideal probe. It can be seen that the modeled image fits the experimental data in a satisfactory way. For the complete NSOM geometry computations, the outer geometry of the probes was taken from the SEM measurements (three images from x, y and

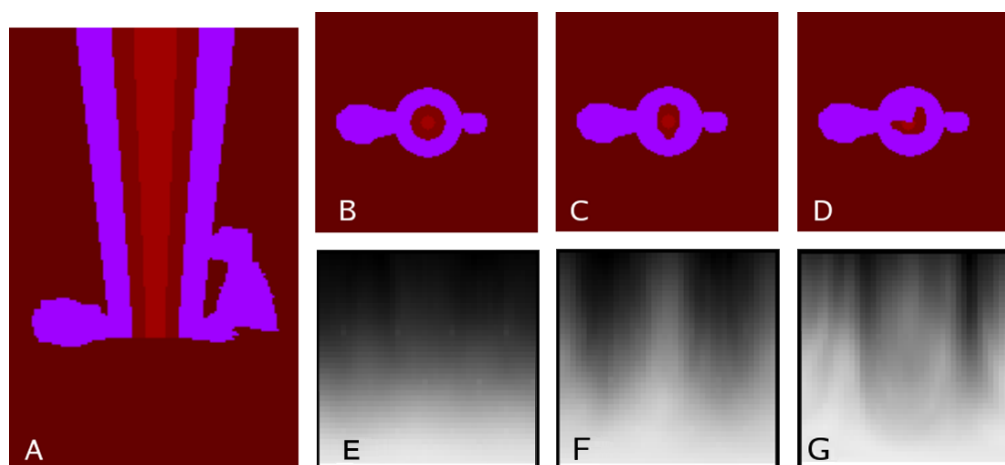


**Figure 3.** Modeled far-field probe radiation diagrams for different probe geometries. (A) probe geometry cross-section in x axis, (B–D) probe geometry cross-sections in z axis, (E–G) corresponding far-field radiation diagrams. This figure is available in colour online at [www.interscience.wiley.com/journal/sia](http://www.interscience.wiley.com/journal/sia).

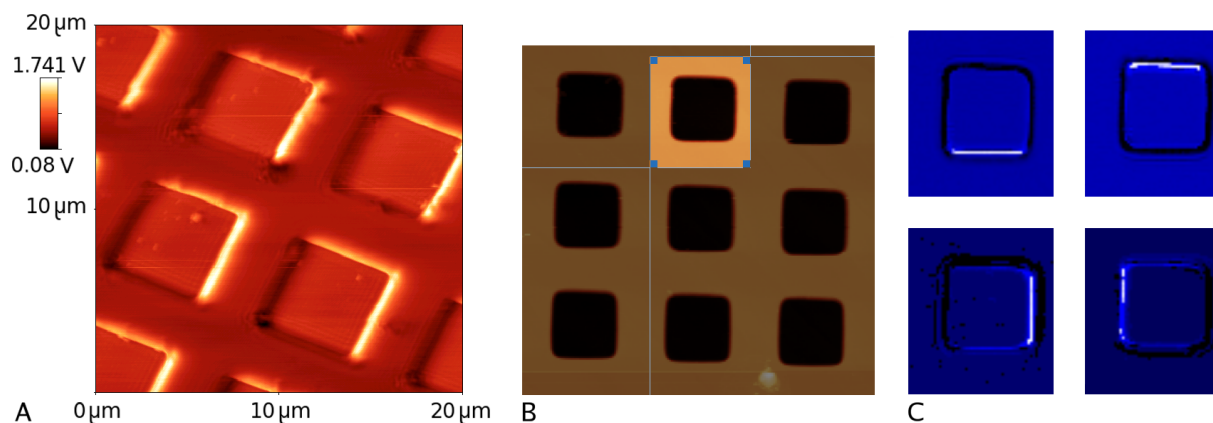


**Figure 4.** (A) Measured NSOM reflection image, (B) AFM topography used for simulation and (C) simulated NSOM reflection images of calibration grating part (four different orientations of the far-field detector—up, down, left and right oriented with respect to the image,  $45^\circ$  from the surface normal). All the gratings have the same pitch (AFM topography data are used for the computations). Intensity (false color scale) is plotted in relative units. This figure is available in colour online at [www.interscience.wiley.com/journal/sia](http://www.interscience.wiley.com/journal/sia).

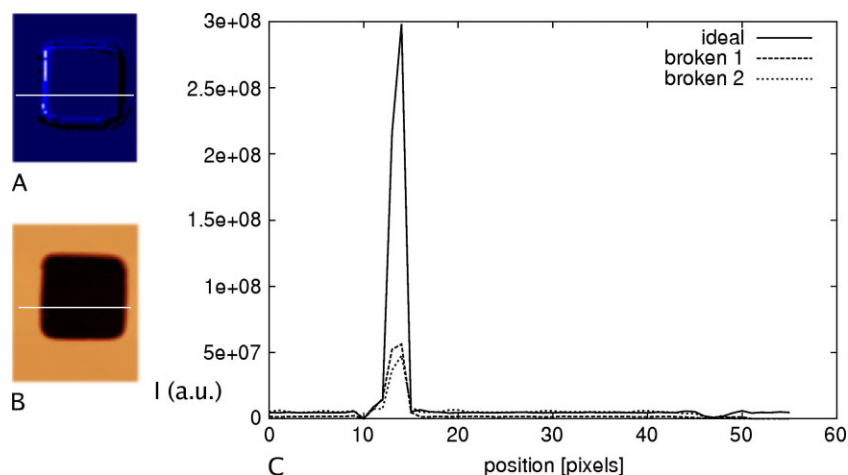


**Figure 5.** (A) Simulated NSOM image with selected profile (the depression presented in Fig. 4(C)), (B) AFM data used for simulation with selected profile, (C) intensity profile obtained from the simulated NSOM image for an ideal and two different nonideal probes. The depression size is 4.5  $\mu\text{m}$ , depth is 180 nm. This figure is available in colour online at [www.interscience.wiley.com/journal/sia](http://www.interscience.wiley.com/journal/sia).

z direction were taken for each studied probe); meanwhile, the inner geometry was guessed to make the best fit to the far-field radiation experimental data. The fit procedure is illustrated in Fig. 3, wherein the models of different inner geometries of the probe (with outer geometry based on SEM measurements) are presented, together with the corresponding far-field data. The far-field radiation diagrams measurement method can be therefore considered as being a simple method for the evaluation of the probe quality within NSOM measurements. The inner and outer geometry determined by both SEM and far-field radiation measurements was used for further modeling of complete NSOM tip-sample geometry to validate the modeling approach.

In Fig. 4, measured (A) and modeled (C) NSOM reflection images of calibration grating parts are presented. Topography data for NSOM modeling were taken from atomic force microscopy (AFM) measurement (highlighted part of Fig. 3(B)) to prevent a doubling effect of NSOM-tip convolution. The AFM-tip size was considered as negligible compared to the NSOM tip. We can see the main effects typical for NSOM measurements – the effect of the far-field detector position with respect to the sample orientation and the effect of steep slopes (changes in the tip-sample distance). Note that there is also an optical contrast between the silicon and silicon dioxide parts of the sample; however, as this contrast is much smaller than the artefacts intensity it cannot be seen on the presented images easily (both measured and simulated).

In Fig. 5, the effects of a broken tip are presented on a single profile over a grating protrusion. A broken tip is represented in this simulation by an artificial gap of given size oriented in the x-direction (direction of the simulated scans presented in Fig. 5) that is added to the circular tip aperture. This corresponds to a very common variant of broken-tip aperture (as known from SEM measurements). It can be seen that the shown topography artefacts are strongest when all the light passes through the aperture (ideal probe). This corresponds to experimental practice, when both the resolution and the number of typical artefacts decreases with broken probes.

## Conclusion

In this article, we have presented the results of experimental measurement and theoretical modeling of far-field radiation of

NSOM probes. It is shown, that using the FDTD method the probe inner and outer geometry can be modeled in a satisfactory way. Using a combination of SEM and far-field radiation measurements, we are able to characterize NSOM probes roughly. Of course, the information obtained from the far-field radiation measurements cannot be complete; however, the presented method can be used for daily checking of the NSOM probe quality or its changes (simply by monitoring changes of the far-field radiation patterns).

Moreover, we have presented the results of modeling the complete tip-sample geometry and resulting simulated NSOM images compared with real measurements. Typical effects observed within the reflection NSOM measurements are seen both on the modeled and on the real images. The tip-characterization method and FDTD modeling can be therefore used for further analysis of local optical properties.

## Acknowledgements

This work was supported by the Ministry of Industry and Trade of the Czech Republic under contract FT-TA3/142 and by Czech office for Standards, Metrology and Testing under contract III/25/07.

## References

- [1] Paesler MA, Moyer PJ. *Near-field Optics, Theory, Instrumentation and Applications*. John Wiley & Sons: New York, 1996.
- [2] Rosenberger A, Münnemann A, Kiendl F, Güntherodt G, Rosenbusch P, Bland JAC, Eggers G, Fumagalli P. *J. Appl. Phys.* 2001; **89**: 7727.
- [3] Hecht B, Sick B, Wild UP, Deckert V, Zenobi R, Martin OJ, Pohl DW. *J. Chem. Phys.* 2000; **112**: 7761.
- [4] Hecht B, Bielefeldt H, Inoué Y, Pohl DW, Novotny L. *J. Appl. Phys.* 1997; **81**: 2492.
- [5] Weston KD, DeAro JA, Buratto SK. *Rev. Sci. Instrum.* 1996; **67**: 2924.
- [6] Fenwick O, Latini G, Caciulli F. *Synth. Met.* 2004; **147**: 171.
- [7] Gucciardi PG, Colloci M. *Appl. Phys. Lett.* 2001; **79**: 1543.
- [8] Martin OJ, Girard Ch, Detreux A. *J. Opt. Soc. Am. A* 1996; **13**: 1801.
- [9] Simpson SH, Hanna S. *Opt. Commun.* 2005; **256**: 476.
- [10] Krug JT, Sanchez EJ, Sunney Xie X. *J. Chem. Phys.* 2002; **116**: 10895.
- [11] Ramahi OM. *IEEE Trans. Antennas Propagat.* 1997; **45**: 753.